

# Potential Poroelastic Triggering of the 2020 M5.0 Mentone Earthquake in the Delaware Basin, Texas, by Shallow Injection Wells

by Xinyu Tan\* and Semechah K. Y. Lui\*

Department of Chemical and Physical Sciences, University of Toronto Mississauga, 3359  
Mississauga Road, Mississauga, Ontario, Canada, L5L 1C3, [xy.tan@mail.utoronto.ca](mailto:xy.tan@mail.utoronto.ca),  
[semechah.lui@utoronto.ca](mailto:semechah.lui@utoronto.ca) (X.T., S.K.Y.L.)

Corresponding author: [xy.tan@mail.utoronto.ca](mailto:xy.tan@mail.utoronto.ca)

\*Also at Department of Earth Sciences, University of Toronto, 22 Russell Street, Toronto,  
Ontario, Canada, M5S 3B1.

## KEY POINTS:

- The M5 Mentone event occurred on a south-facing normal fault with a strike and dip of 81 and 52 degrees.
- Shallow injections may have promoted the occurrence of the mainshock by poroelastic stress perturbations.
- Rock properties of the injection layer can notably affect coupled pore pressure and stress perturbations.

## ABSTRACT

The Delaware Basin in Texas, one of the largest oil and gas production sites in the US, has been impacted by widespread seismicity in recent years. The M5.0 earthquake that occurred in March 2020 near the town of Mentone is one of the largest induced earthquakes recorded in this region. Characterizing the source parameters and triggering mechanism of this major event is imperative to assess and mitigate future hazard risk. A former study showed that this event may be attributed to the deep injection nearby. Interestingly, the earthquake is located in proximity to shallow injection wells with much larger total injection volume. In this study, we investigate the role of these shallow injection wells in the triggering of the M5.0 event despite their farther distance from the mainshock. We perform source-parameter inversion and earthquake relocation to determine the precise orientation of the south-facing normal fault plane where the mainshock occurred, followed by fully coupled poroelastic stress modeling of the change of Coulomb Failure Stress ( $\Delta CFS$ ) on the fitted fault plane caused by shallow injection in the region. Results show that shallow wells caused up to 20 kPa of  $\Delta CFS$  near the mainshock location, dominated by positive poroelastic stress change. Such perturbation surpasses the general triggering threshold of faults that are well aligned with the local stress field and suggests the nonnegligible role of these shallow wells in the triggering of the mainshock. We also discuss the complex effect of poroelastic stress perturbation in the subsurface and highlight the importance of detailed geomechanical evaluation of the reservoir when developing relevant operational and safety policies.

## INTRODUCTION

Underground fluid injection, such as hydraulic fracturing, wastewater disposal, geothermal utilization and carbon sequestration, has led to a dramatic increase of seismicity globally (Ellsworth, 2013; Bao & Eaton, 2016; Keranen & Weingarten, 2018). In the Delaware Basin, Texas, the increase of oil and gas related activities has resulted in widespread seismicity in recent years (Skoumal et al., 2020, 2021; Zhai et al., 2021). Between 2014 and 2018, 24 sizable earthquakes ( $M \geq 3$ ) have occurred in the Basin, while only 20 were reported in the previous 25 years combined (1970 – 2014) (Skoumal et al., 2020). On March 26, 2020, a M5.0 event occurred near Mentone and close to the border of Reeves County and Culberson county, which is one of the largest induced earthquakes in Texas to date (Figure 1).

For induced events that occur on faults close to injection operations, their activation is typically attributed to the build-up of pore pressure from neighboring wells (Keranen et al., 2013), though it has also been suggested that pore fluid can diffuse over large distances and trigger earthquakes remotely (Keranen et al., 2014; Yeck et al., 2016). For the Mentone earthquake, there are only 4 shallow injection wells within 5 km, all with small cumulative injection volume ( $< 6 \times 10^6$  BBLs). Wells with much larger volume are located at distances between 10 km and 25 km (Figure 1).

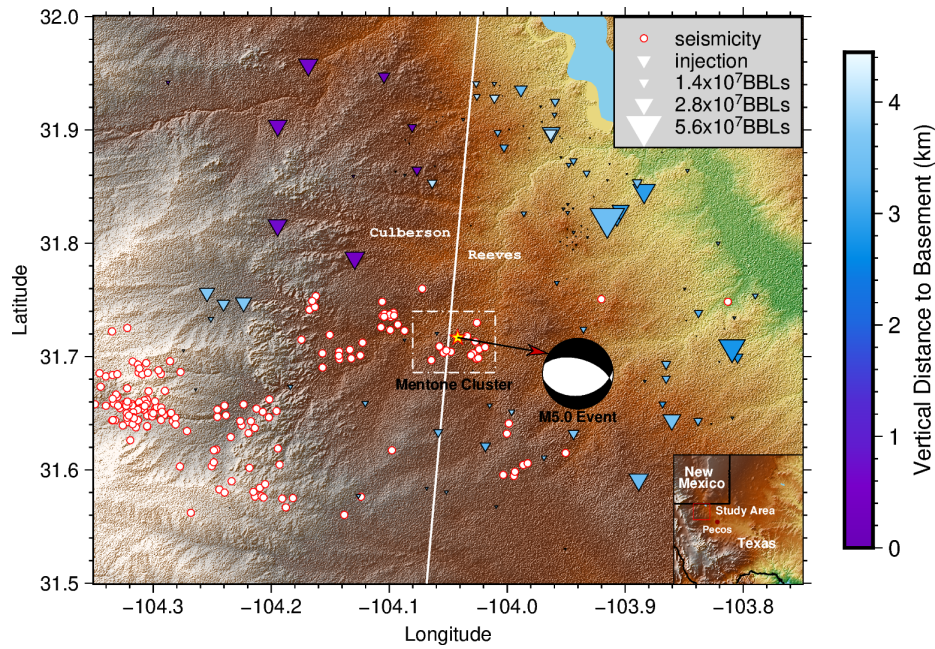


**Figure 1.** Location of injection wells (inverted triangles) and seismic events (red circles) within 25 km of the mainshock (yellow star). The size and color of the inverted triangles are proportional to the injection volume and the vertical distance between the injection wells and the basement, respectively. The Mentone (mainshock) cluster is enclosed in the white dashed rectangle. The bottom-right inset shows the location of the study area (red rectangle) in western Texas. Purple inverted triangles are deep injection wells included in the study by Tung et al. (2021).

Tung et al. (2021) attributed the cause of the M5.0 event to the fluid diffusion from deep injection wells in the highly permeable Ellenburger group (limestone layer) located to the northwest of the mainshock, assuming a hydraulic connection between the limestone layer and the basement. Interestingly, apart from these deep wells, there are also a lot of shallow injection wells within 25 km of the mainshock with much larger total injection volume, approximately five times larger than that of the deep wells (Figure 2). In particular, shallow wells to the northeast of the mainshock

alone have contributed a volume 2.5 times larger than that of the deep injection wells, which is also the largest among the four quadrants around the mainshock. These shallow wells, despite their relatively large epicentral distance ( $> 5$  km), may entertain the possibility of remote triggering due to their high injection volume (Goebel et al., 2017; Goebel & Brodsky, 2018; Zhai et al., 2021). Motivated by this, we investigate in this study the potential contribution of these shallow injection wells to the Mentone earthquake and the possible triggering mechanisms. We analyze their perturbations in pore pressure and coupled poroelastic stress caused on the reactivated basement fault without assuming any hydraulic connection in the reservoir.

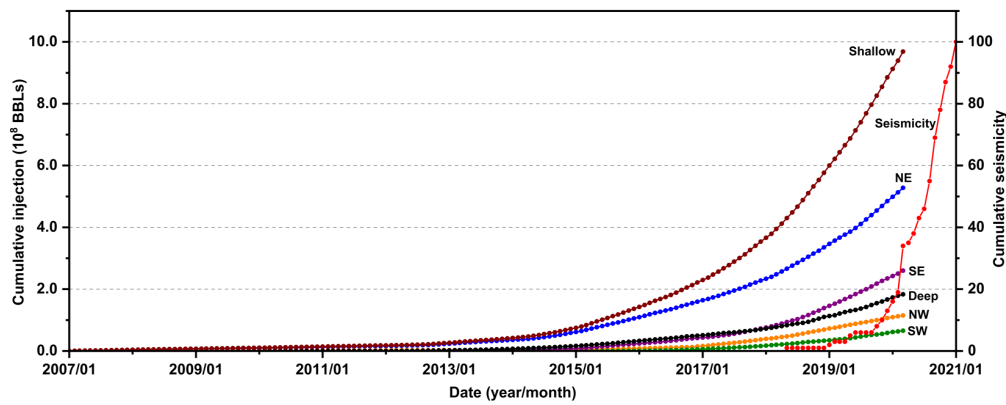


**Figure 2.** Cumulative seismicity within 25 km of the mainshock (red curve; up to January 2021) and injection volume of injection wells up to the occurrence of the Mentone event in March 2020. “Shallow” represents cumulative injection volume of all shallow wells within 25 km of the mainshock, and “Deep” represents deep injection wells used in Tung et al. (2021). “NE”, “NW”, “SW”, and “SE” represent individual cumulative injection volume of shallow wells in the northeast, northwest, southwest, and southeast quadrant, respectively.

Previous studies showed that the normal and shear stress on the fault plane are highly sensitive to the location and orientation of the fault (Deng et al., 2020; Lim et al., 2020), hence, correctly resolving the orientation of the fault plane is an imperative step. In this work, we first perform source parameter inversion on the mainshock and selected adjacent events considering their time and location proximity to the mainshock. Then we constrain the fault plane orientation by fitting relocated events. Lastly, we conduct fully-coupled poroelastic modeling to calculate the change of the Coulomb failure stress ( $\Delta CFS$ ) on the fitted fault plane and investigate the effects of shallow injection wells on the occurrence of the M5.0 event. In the following sections, we first introduce the methods and discuss the results on earthquake relocation and source parameter (focal mechanism, depth) inversion. Next, we detail the methods in conducting the poroelastic modeling and the analysis result. In the Discussion section, we further elaborate on the validation of triggering by shallow injection based on the spatiotemporal distribution of nearby seismicity, as well as the complexity in assessing the role of poroelastic triggering.

## SOURCE PARAMETER INVERSION AND EARTHQUAKE RELOCATION

### Data and Methods

To better constrain source parameters and identify events that potentially occurred on the mainshock fault plane, the Cut and Paste (CAP) method (Zhao & Helmberger, 1994) is utilized to perform the focal mechanism and depth inversion. Through fitting synthetic and observed waveforms of segmented body and surface waves, the CAP method is capable of resolving the optimal source mechanism by grid-searching the seismic moment ( $M_0$ ), focal mechanism, and depth of the target event with minimum misfit. Here we use the frequency-wavenumber method

to compute the Green's functions as 1D synthetic waveforms input for the inversion (Zhu & Rivera, 2002). The 1D velocity model used in our inversion is derived jointly from sonic velocity logs of a well in the Delaware Basin (Sheng et al., 2022) and the central United States velocity model (CUS). For details of the model, see Figure S1 in supplemental material to this article.

In terms of events selected for focal mechanism inversion, apart from the small cluster containing the mainshock (the Mentone cluster in Figure 1), there are also some neighboring events located between 5 and 10 km to the west and northwest of the mainshock. To determine whether these events occurred on the mainshock fault plane, we conducted focal mechanism inversion on seven events with  $M \geq 3.0$ , three of which from the Mentone cluster and the other four from the neighboring clusters (Table 1).

**Table 1.** Catalog information of selected events obtained from IRIS.

Event	Catalog time	Latitude	Longitude	Magnitude	Focal Depth (km)
01	2020-03-26 15:16:27	31.7168	-104.0419	5.0	9.51
02	2020-03-26 08:52:41	31.7065	-104.0237	3.8	5
03	2020-03-29 01:27:06	31.7029	-104.0288	3.5	5
04	2020-09-18 21:48:27	31.7061	-104.1334	3.5	5
05	2020-10-28 14:07:37	31.7011	-104.1244	3.7	5
06	2020-11-15 15:44:53	31.7349	-104.0986	3.3	5
07	2020-09-03 03:52:27	31.7360	-104.1057	3.0	8.03

Apart from using focal mechanism information to constrain the orientation of the mainshock fault plane, we also relocate earthquakes near the M5.0 event to minimize hypocenter uncertainty and to allow for individual fault structures to be delineated, which is conducive to subsequent stress and pressure calculation. While many wells within 25 km are to the northeast of the mainshock, most seismicity are located to the southwest end of the mainshock (Figure 1). Here we perform HypoDD relocation (Waldhauser & Ellsworth, 2000) on earthquakes with azimuths to the mainshock ranging between  $225^{\circ}$  and  $325^{\circ}$ , which include the Mentone cluster and two other clusters aforementioned (Figure 3). 41 stations with epicentral distance between 20 and 230 km are selected for the analysis (Table S1).

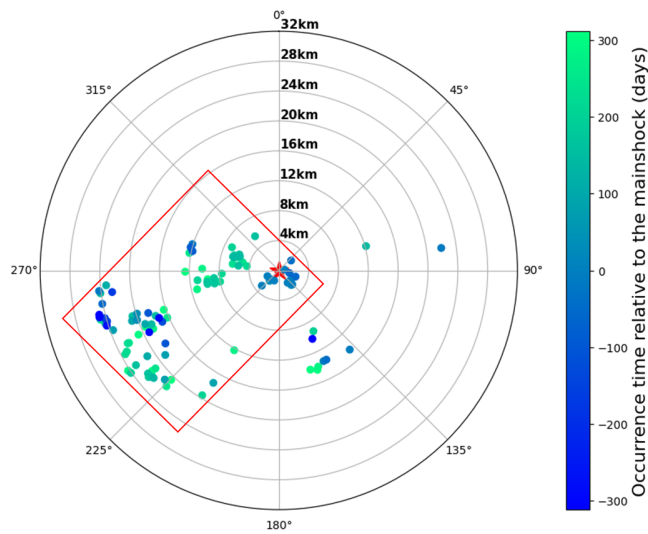


**Figure 3.** Radial plot displaying events located within 25 km from the mainshock (the red star). Selected events for hypoDD relocation are enclosed within the red rectangle. Colorbar indicates the relative occurrence time of earthquakes to the mainshock.

We first use PhaseNet (Zhu & Beroza, 2019) to generate phase arrival time automatically. Then, to better constrain the accuracy of relocation result, we calculate the cross correlation of data with

ObsPy's cross-correlation pick correction function following Deichmann & Fernandez (1992) and select data with correlations coefficient  $> 0.75$  for hypoDD relocation. An example of phase pick output from PhaseNet and parameters used in HypoDD relocation are included in Figure S2 and Table S2, respectively. We also perform jackknife resampling to estimate the uncertainty (Table S3).

## Results

The CAP inversion parameters and results are listed in Table 2. Resolved focal mechanisms (strike, dip, rake) of the M5.0 event are  $288^\circ$ ,  $51^\circ$ ,  $-67^\circ$  and  $74^\circ$ ,  $44^\circ$ ,  $-115^\circ$ , respectively, and the optimal focal depth is 6.6 km. Figure 4 shows the comparison between synthetic and observed waveforms of the M5.0 event at the optimal depth, the cross-correlation values of each waveform pair, and the relative misfit error at different focal depths. Inversion results of other selected events are in Figures S3 – S8. Based on similarity in focal mechanisms, events 01-07 likely belong to three different clusters: Cluster I include events 01 (mainshock), 02 and 03. Events 04 and 05 belong to cluster II, and events 06 and 07 to Cluster III. Events 04-07 likely occurred on fault planes different from the mainshock fault plane, considering their focal mechanism as well as relative time and location to the Mentone cluster.

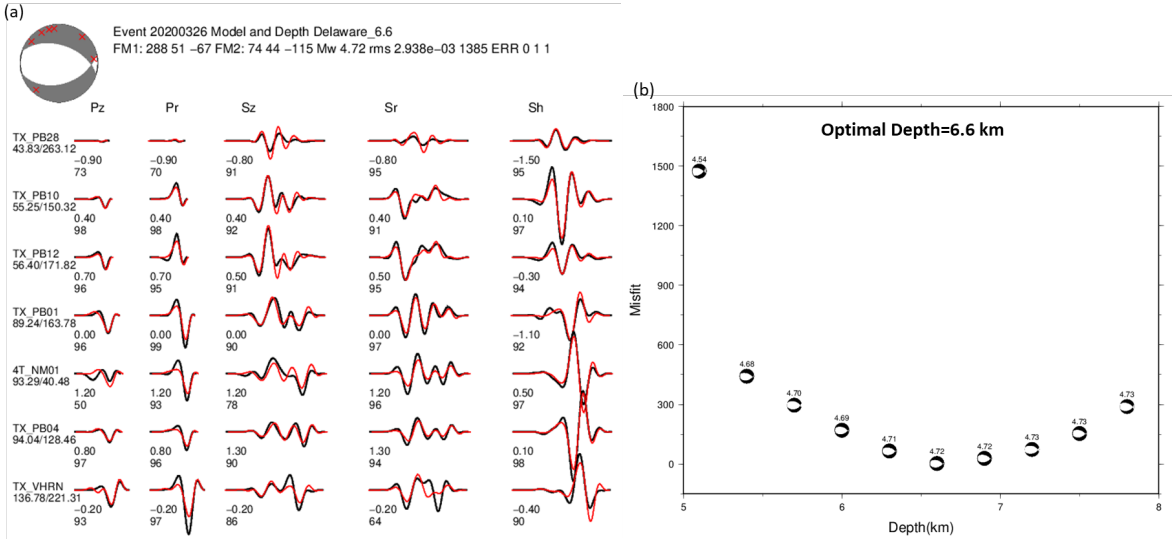
Similar to focal mechanism inversion results, HypoDD relocation results also point to three separate earthquake clusters (Figure 5). Compared with catalog locations, relocated events within each cluster are positioned closer to one another. The orientations of the respective fault planes are

approximated in 3D (Figure 6). The fitted strike/dip angles of clusters I, II and III are  $81^{\circ}/52^{\circ}$ ,  $95^{\circ}/58^{\circ}$ , and  $113^{\circ}/73^{\circ}$ , respectively. Although these three clusters share similar dip angles, there is obvious disparity among their strike angles and occurrence time relative to the mainshock. The fitted fault plane of cluster I shares similar strike and dip angles with the M5.0 mainshock and is regarded as the fault plane on which the earthquake occurred. We also applied the Jackknife method for the uncertainty estimation of the fault orientation of each cluster (Table S3). Overall, with 1000, 2000 and 3000 times of jackknife sampling, the standard deviation of the strike angle of fitted fault planes is smaller than that of the dip angle, which is reasonable with a generalized 1D velocity model. Besides, the relative standard deviation of the fitted fault plane I ( $\sim 1\%$  for strike and  $\sim 12\%$  for dip angles) is the smallest among the three fitted fault planes (Strike/Dip =  $\sim 4\%/\sim 15\%$  for fault plane II and  $\sim 9\%/\sim 25\%$  for fault plane III). The results strengthen our confidence in using the fitted fault plane I as the mainshock fault plane to calculate the injection-induced fully coupled poroelastic perturbations.

**Table 2.** Parameters used in the CAP inversion and inverted focal mechanisms. Time windows for Pnl and S wave segments used in CAP are 35s and 70s, respectively.

Event	Filtered frequency range (Hz)		Focal Mechanism from CAP (strike, dip, rake)		Optimal depth (km)
	Pnl waves	S waves			
01	0.02-0.10	0.02-0.10	$288^{\circ}, 51^{\circ}, -67^{\circ}$	$74^{\circ}, 44^{\circ}, -115^{\circ}$	6.6
02	0.05-0.20	0.05-0.20	$280^{\circ}, 49^{\circ}, -58^{\circ}$	$56^{\circ}, 50^{\circ}, -121^{\circ}$	5.4
03	0.10-0.20	0.10-0.20	$299^{\circ}, 40^{\circ}, -46^{\circ}$	$67^{\circ}, 62^{\circ}, -120^{\circ}$	5.4
04	0.12-0.22	0.10-0.20	$322^{\circ}, 39^{\circ}, -35^{\circ}$	$80^{\circ}, 68^{\circ}, -123^{\circ}$	5.4

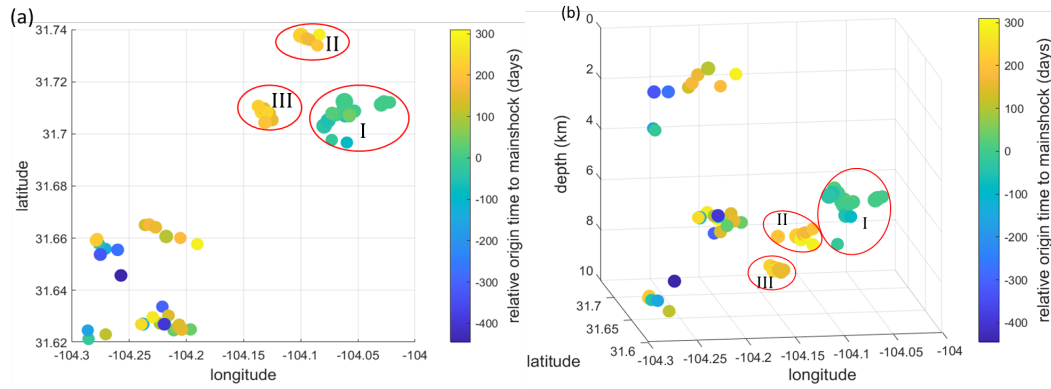
05	0.12-0.22	0.10-0.20	323°, 43°, -42°	86°, 62°, -124°	5.4
06	0.12-0.25	0.15-0.30	17°, 57°, -15°	115°, 77°, -146°	3.3
07	0.08-0.22	0.10-0.25	10°, 66°, -14°	105°, 77°, -155°	5.1



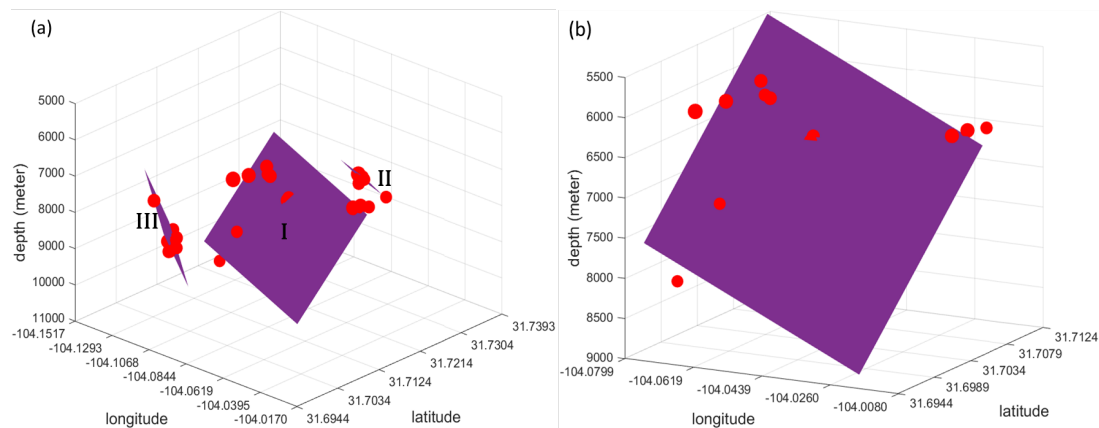
**Figure 4.** (a) Synthetic (red) and recorded (black) waveforms have the highest correlation at the optimal depth of 6.6 km for the M5.0 event. The numbers below the waveforms are optimal shift time (in second) and cross correlation coefficient, respectively. (b) Relative misfit error of the mainshock inversion at different focal depths. The number above each focal mechanism symbol is the best-fit event magnitude.

The mainshock depth after relocation (6.7 km) is considerably shallower than the IRIS catalog depth (9.51 km, Table 1), but is consistent with the centroid depth obtained from the independent CAP inversion (6.6km, Table 2) and from the TexNet earthquake catalog (7.1 km), which strengthens our confidence in the HypoDD relocation results. It should be noted that even though

the 1D velocity model used for the source inversion may be simplified or imperfect, the CAP approach is capable of generating accurate source estimates because differential time shifts are allowed among the different body and surface waveform segments. Large shift in the focal depth after relocation is also shown in Sheng et al. (2022) for events in the neighboring region (Reeves-Peco County) and can be attributed to the sparse distribution of seismic stations and difference in the velocity model.



**Figure 5.** (a-b) 2D and 3D view of the relocated events, respectively. Colorbar represents their event time relative to that of the mainshock. Clusters I, II and III are circled in red.



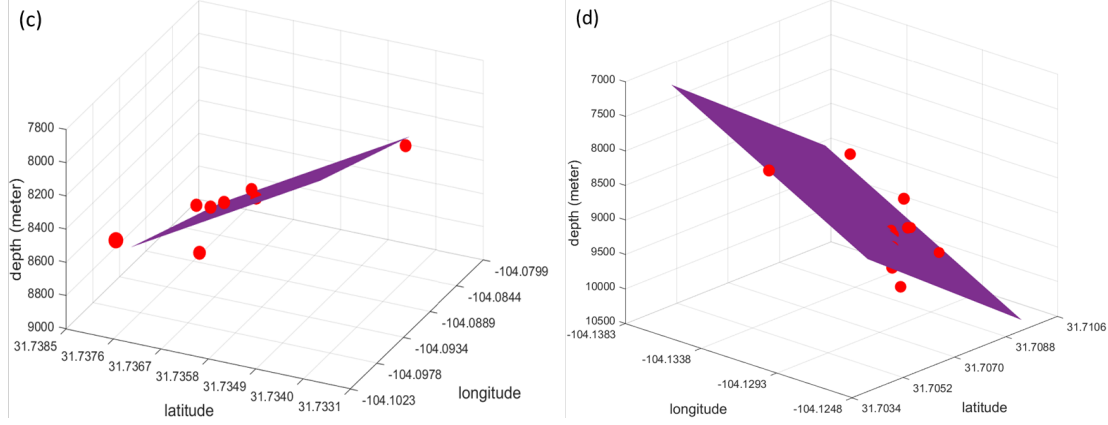


**Figure 6.** (a) Fitted fault planes of clusters I, II and III based on HypoDD results. (b)-(d) Zoomed-in plots of individual clusters I, II, and III, and their corresponding fitted planes.

## FULLY-COUPLED MODELING OF POROELASTIC RESPONSE

### Data and Method

With the relocated hypocenter and fitting fault plane, we compute the temporal change of pore pressure and poroelastic stress in the basement near the mainshock location due to shallow injections. We adopt the open-source package POEL (PoroELastic diffusion and deformation), a semi-analytical method governed by the following equations (Wang & Kümpel, 2003):

$$(\lambda + 2\mu) \nabla (\nabla \cdot \mathbf{u}) - \mu \nabla \times (\nabla \times \mathbf{u}) - \alpha \nabla p = \mathbf{f}(\mathbf{x}, t) \quad (1)$$

$$Q^{-1} \frac{\partial p}{\partial t} + \alpha \frac{\partial}{\partial t} \nabla \cdot \mathbf{u} - \chi \nabla^2 p = q(\mathbf{x}, t) \quad (2)$$

Where  $\lambda$  and  $\mu$  are the Lamé parameters,  $\mathbf{u}$  is the displacement vector,  $\alpha$  is the Biot's coefficient of effective stress,  $p$  is pore pressure,  $\mathbf{f}(\mathbf{x}, t)$  is the body force on the rock matrix,  $Q^{-1}$  is bulk

compressibility,  $\chi$  is Darcy conductivity, and  $q(\mathbf{x}, t)$  is the injection source. Both  $\mathbf{f}(\mathbf{x}, t)$  and  $q(\mathbf{x}, t)$  are functions of space ( $\mathbf{x}$ ) and time ( $t$ ). Equation (1) depicts the solid deformation coupled with the change of pore pressure due to fluid injection, which is the fluid-solid coupling. Equation (2) depicts the fluid mass conservation coupled from the solid deformation, which is the solid-fluid coupling (Chang & Segall, 2016; Zhai et al., 2021).

Through utilizing the analytical solution from Rudnicki (1986) for equation (1) and (2) in the homogeneous whole space, POEL models the pore pressure and strain tensor of rock matrix caused by time-varying injection in a cylindrically symmetrical layered poroelastic half-space (schematic illustration shown in Figure 7).

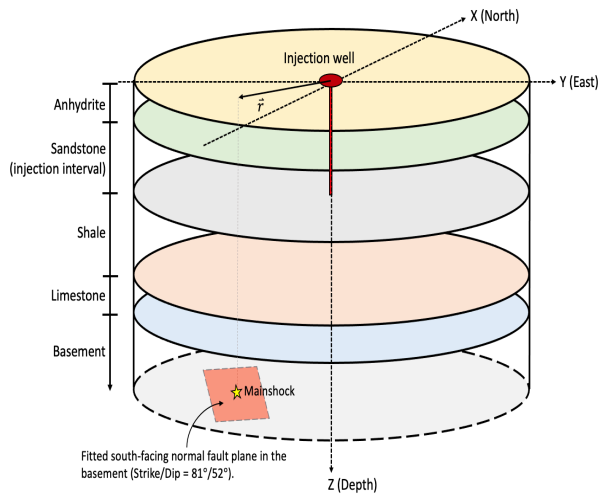


**Figure 7.** Schematic illustration of simulation domain in POEL (dimensions not to scale). Our model comprises of five geologic layers, with injection occurring within the sandstone layer. Coulomb failure stresses are calculated on the fitted fault plane near the mainshock hypocenter location.

229

230 In our simulation, boundary-value-problem mode is selected with an initial pore pressure of 0 MPa  
 231 (Barbour et al., 2017). The input geomechanical parameters are shear modulus  $\mu$ , Poisson's ratio  
 232  $\nu$  of drained condition and  $\nu_u$  of undrained condition, Skempton coefficient  $B$  and hydraulic  
 233 diffusivity  $D$ . Other coupled poroelastic parameters, including  $\lambda$ ,  $\alpha$ ,  $Q^{-1}$  and  $\chi$  can be obtained  
 234 with these five input parameters (Wang & Kümpel, 2003; Barbour et al., 2017):

$$235 \quad \lambda = \frac{2\nu\mu}{1-2\nu} \quad (3)$$

$$236 \quad \alpha = \frac{3(\nu_u - \nu)}{(1-2\nu)(1+\nu_u)B} \quad (4)$$

$$237 \quad Q^{-1} = \frac{9}{2} \frac{(1-2\nu_u)(\nu_u - \nu)}{(1-2\nu)(1+\nu_u)^2 \mu B^2} \quad (5)$$

$$238 \quad \chi = \frac{9}{2} \frac{(1-\nu_u)(\nu_u - \nu)D}{(1-\nu)(1+\nu_u)^2 \mu B^2} \quad (6)$$

239 We implement a geological model composed of five layers: (from top to bottom) anhydrite,  
 240 sandstone, shale, limestone, and basement (Table 3; cf., Tung et al., 2021). All shallow and deep  
 241 injections within 25 km from the mainshock occur in the high permeable sandstone and limestone  
 242 layers, respectively (Figure S9 and Table S4). For geomechanical parameters, we apply those from  
 243 Tung et al. (2021), except for  $D$  of the anhydrite/halite and shale layers, as well as  $\nu_u$  and  $B$  of the  
 244 shale layer, which are chosen from other relevant studies (Beauheim & Roberts, 2002; Makhnenko  
 245 et al., 2011; Suarez-Rivera & Fjær, 2013; Li et al., 2020; Zhai et al., 2021). To this end, we also  
 246 conduct a sensitivity study on the geomechanical parameters, which is detailed in the Results  
 247 section below.

Based on results from POEL, we perform tensor transformation to obtain the local normal stress and shear stress on the fault plane where the mainshock occurred (Zoback, 2010) and analyze the Coulomb failure stress change ( $\Delta CFS$ ) on the fitted fault plane near the mainshock location. The Coulomb failure theory (Jaeger & Cook, 1979) states that  $\Delta CFS$  is defined as:

$$\Delta CFS = \Delta\tau + \mu(\Delta\sigma + \Delta p) \quad (7)$$

where  $\Delta\tau$  and  $\Delta\sigma$  represent the change of shear stress (positive for promoting failure) and normal stress (positive for unclamping the fault),  $\Delta p$  represents the change of pore pressure on the fault, and  $\mu$  is the coefficient of friction. Fault failure is promoted when  $\Delta CFS$  is positive, and vice versa. From equation (7), changes in direct pore pressure and the resulting poroelastic stress separately contribute to  $\Delta CFS$ .

**Table 3.** Geological model used in our analysis.

Rock type	Depth (m)	$\mu$ (Pa)	$\nu$	$\nu_u$	$B$	$D$ ( $m^2 s^{-1}$ )
Anhydrite, halite	0 - 700	5.96E+09	0.26	0.40	0.86	0.00002
Sandstone	700 - 2500	26.91E+09	0.26	0.36	0.58	0.64000
Shale	2500 - 4500	26.91E+09	0.26	0.37	0.60	0.00002
Limestone	4500 - 5200	12.10E+09	0.26	0.36	0.65	1.00000
Basement	5200 -	30.86E+09	0.26	0.33	0.80	0.00002

For the poroelastic modeling, we select wells within 25 km of the mainshock with relatively large injection volume and divide them into four groups based on their locations from the mainshock, i.e. the northeast, southeast, southwest and northwest quadrants (Table S4). The selected wells account for 40-70% of the total injection volume in their respective quadrants. We compute their pressure and stress perturbation on the fitted fault plane separately and then combine their perturbations to obtain the overall contribution from all shallow injection wells. To simplify the calculation process, wells within each quadrant that are very close to one another are moved to an averaged location (Figure S10 and Table S5). Note that all the wells undergoing this simplification procedure are within 1.5 km from their average location. We examine the robustness of this averaging approach and confirm that the difference in pore pressure at the mainshock location caused by the simplification is minimal, i.e. ~5% of the total pore pressure perturbation. Wells at a farther distance apart are treated as individual wells at their true locations.

## Results

The time evolution of the total monthly injection rate of selected wells, as well as the resulted change in pore pressure, normal stress, shear stress, poroelastic stress and  $\Delta CFS$  are displayed in Figure 8. Detailed results of individual wells are listed in Table S4. It is found that at the early stage of the injection (before 2015) with low injection rate, pressure and stress perturbations near the mainshock are pretty small due to the large distance (10-20 km) between selected wells and the mainshock. Starting in 2015, with increasing injection rate, the total pore pressure perturbation near the mainshock transitioned from positive (encourage fault slip) to negative (inhibit fault slip), and the negative pore pressure increases with the injection rate. This phenomenon is mainly caused

by the coupling effect of the poroelastic stress on the pore pressure. As the thick shale layer below the shallow injection sandstone layer has low permeability, direct pore pressure change due to percolation of injected fluid through the shale layer is unlikely. According to Chang & Segall (2016), injected fluid causes expansion of the layer below the injection layer, which subsequently compacts the layer at further distances. The boundary of expansion and compaction is determined by rock properties and injection parameters, and the zone of expansion gradually moves outward as injection continues. In the beginning, due to low injection rate and large distance between the injection wells and the mainshock, the basement rock layer near the mainshock location underwent compaction and, hence, the change in pore pressure remained positive until early 2018. As injection continued, the expansion region continued to move outward, and pore pressure eventually transitioned from positive to negative. Both normal and shear stresses increase throughout the entire injection period and they increase more rapidly with the rise of injection rate. The resulting poroelastic stress change reaches about 23 kPa at the time of the mainshock. Since the value of the pore pressure change at the mainshock location is negative, the positive  $\Delta CFS$  was solely from poroelastic effects.

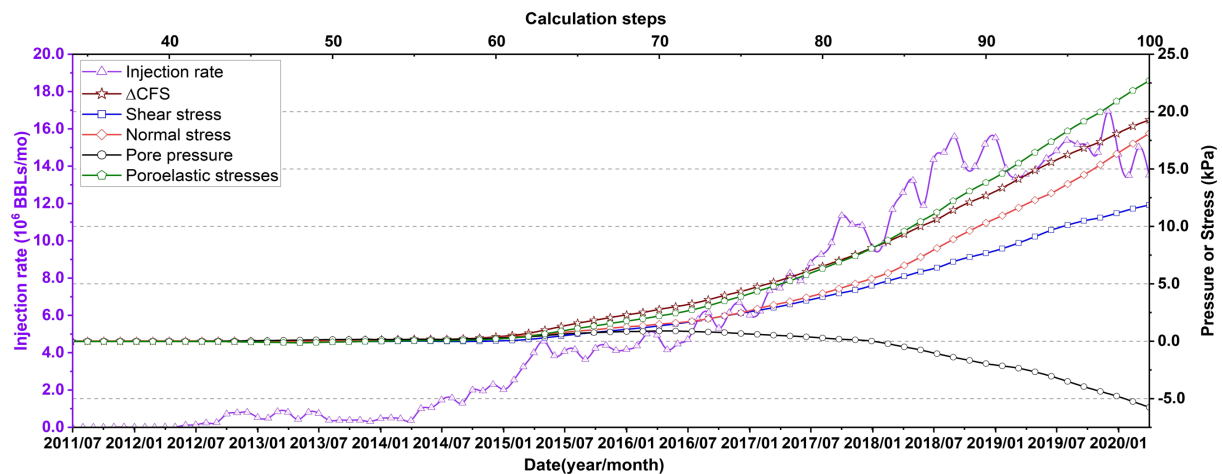


**Figure 8.** Time evolution of the monthly injection rate of selected shallow injection wells, as well as the change in pore pressure, poroelastic stress, normal stress, shear stress and  $\Delta CFS$  on the fitted fault plane near the mainshock location until the occurrence of the M5.0 mainshock.

Overall, the  $\Delta CFS$  increased with an increasing rate and reached  $\sim 20$  kPa when the mainshock occurred, which surpasses the general threshold of 10 kPa for seismic events to be triggered (Rothert & Shapiro, 2007; Deng et al., 2020). Since the fitted fault plane is well aligned with the local stress field, it is possible that even a small perturbation may reactivate the fault (Lund Snee & Dvory, 2020). Furthermore, we only include wells with relatively large injection volumes in our calculation. If we account for the injection volume and location of all shallow wells, the total  $\Delta CFS$  from shallow injection will be larger than 20 kPa. In Tung et al. (2021), it is suggested that the deep injection wells in the Ellenburger group (limestone layer) caused a  $\Delta CFS$  of  $\sim 80$  kPa near the mainshock location, assuming hydraulic connections between the limestone layer and the basement. For comparison, we calculate the pressure and stress perturbations of the deep injection wells to the northwest of the mainshock (Table S6 and Figure S11(a)), assuming no hydraulic connection. Results indicate that  $\Delta CFS$  from deep injection wells would be reduced to  $\sim 1$  kPa at the mainshock location, which is significantly smaller than the contribution from shallow injection wells in any of the four quadrants (Figure S11(b-e)). Therefore, our result implies that the shallow wells in this region can serve as the main driver of the M5.0 Mentone earthquake through poroelastic stress increase.

To test the robustness of our geological model, we also conduct sensitivity analysis on two geological parameters, namely the Skempton coefficient  $B$  of the shale layer ( $B_{shale} = 0.7, 0.8$ , and  $0.9$ ) and the hydraulic diffusivity  $D$  of the sandstone layer ( $D_{sandstone} = 0.1, 0.5$ , and  $1.0$ ). In addition, we test a case with the Skempton coefficient  $B$  and the undrained Poisson's ratio  $\nu_u$  of the shale layer identical to those used in Tung et al. (2021). 10 of the shallow injection wells with larger  $\Delta CFS$  contribution are selected for the analysis (Table S7). With the original set of parameters, these wells cause a cumulative  $\Delta CFS$  of 13.5 kPa. In all the tested scenarios, the cumulative  $\Delta CFS$  value ranges between 11.8 and 17.4 kPa, which remains larger than the general threshold of 10 kPa (Table S8). This strengthens our argument for the long-range poroelastic triggering from shallow injection wells.

## DISCUSSION

Our work shares similar findings with earlier studies regarding the potential significant impact of shallow injection on deep geologic formations via poroelastic stress perturbations (Zhai et al., 2021). In fact, the spatiotemporal evolution of seismic activity near the M5.0 event may also shed lights on the triggering mechanism of events induced in the region. The TexNet earthquake catalogue showed that 330 seismic events were recorded within 10 km of the mainshock between 2017 and 2021, with  $4.9 > M > 0.6$  (Table S9 and Video S1). A seismic swarm initially started to the northeast of the mainshock in late January 2020, then subsequent seismic events mostly occurred along a northeast-southwest-trending fault and exhibited a general migration pattern from northeast to southwest, with the mainshock among them in late March. Almost all the seismic events prior to the mainshock occurred at depths greater than 6 km, which may indicate the

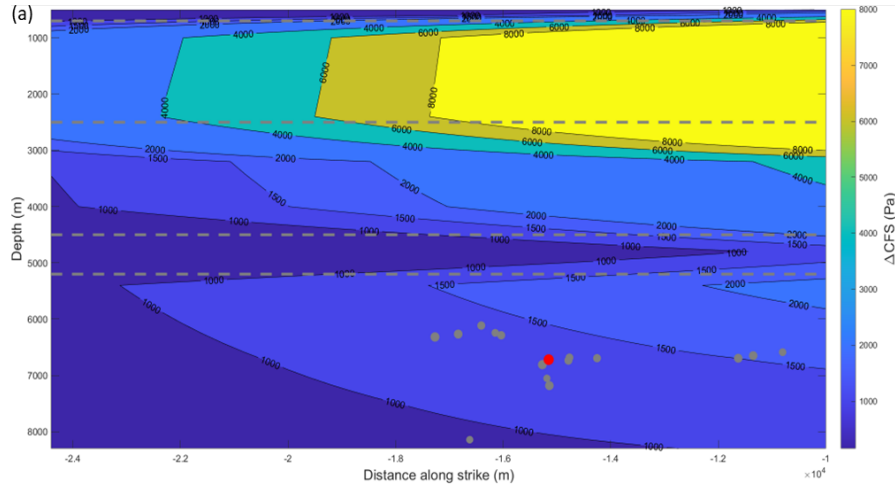
influence of the poroelastic stress perturbation from shallow injection. Besides, it is interesting to note that, within nine months after the M5.0 mainshock, there are two other seismic swarms that occurred to the west and northwest of the mainshock in the basement layer, with average depths > 6 km (clusters II and III in relocation analysis; Video S1). Their occurring after the mainshock and farther distance from the major shallow injection wells suggest that they may also be the result of poroelastic triggering due to shallow injection. Hence, we argue that the spatiotemporal distribution of nearby seismicity confirms the non-negligible role of the poroelastic stress perturbation in this region.

The effect of poroelastic stress in earthquake triggering can be challenging to assess and depends on multiple factors such as the subsurface structure and the injection history. To establish a more detailed comparison of the effects of subsurface hydrogeological properties, we model a shallow-injection scenario (called SI-2 hereafter) and compare that against the original shallow injection scenario (called SI-1 hereafter; Figure S12 and Table S10), with the sole focus on the properties of the injection layer. All parameters are kept constant except for the rock properties of the injection layer: Sandstone in SI-1 and limestone in SI-2. The resulted pore pressure change is smaller in the limestone layer (SI-2) than in the sandstone layer (SI-1) (Figure S13). The change in normal stress, shear stress and  $\Delta CFS$  (Figure 9) near the mainshock location is also smaller in SI-2. While these modeling results are numerically resolved in a multilayer setting, one can also obtain good first-order approximations with the steady-state analytical solutions of injection-induced poroelastic deformation  $\mathbf{u}(\mathbf{x}, t)$  and pore pressure  $p(\mathbf{x}, t)$  in a homogeneous whole space, which are fundamental equations used in the POEL package (Rudnicki, 1986; Wang & Kümpel, 2003):

$$\mathbf{u}(\mathbf{x}, t) = \frac{q_o(1+\nu_u)B}{24\pi(1-\nu_u)D} \frac{\mathbf{x}-\mathbf{x}_s}{R} \quad (8)$$

$$p(\mathbf{x}, t) = \frac{q_o}{4\pi\chi} \frac{1}{R} \quad (9)$$

where  $\mathbf{x}_s$  is the position of the injection source,  $R = |\mathbf{x} - \mathbf{x}_s|$  is the distance between the injection source and the mainshock, and  $q_o$  is a constant injection rate. According to these two equations,  $\mathbf{u}$  and  $p$  primarily depend on properties of the rock medium. Since  $\chi_{limestone}$  is larger than  $\chi_{sandstone}$  ( $4.2 \times 10^{-11} \text{ m}^2/(\text{Pa}\cdot\text{s})$  vs  $1.5 \times 10^{-11} \text{ m}^2/(\text{Pa}\cdot\text{s})$ ), that explains the larger pore pressure change in sandstone (SI-1) than in limestone (SI-2), according to equation (9). In equation (8), the term  $\left[\frac{(1+\nu_u)B}{(1-\nu_u)D}\right]$  for limestone and sandstone are  $1.3812 \text{ s/m}^2$  and  $1.9258 \text{ s/m}^2$ , respectively, and hence the poroelastic deformation is expected to be larger in a sandstone medium. Since SI-1 and SI-2 differs only by the rock type of the injection layer, the overall deformation  $\mathbf{u}(\mathbf{x}, t)$  in the basement layer where the mainshock occurs (6.7 km) would also be larger in SI-1 (Figure S14).



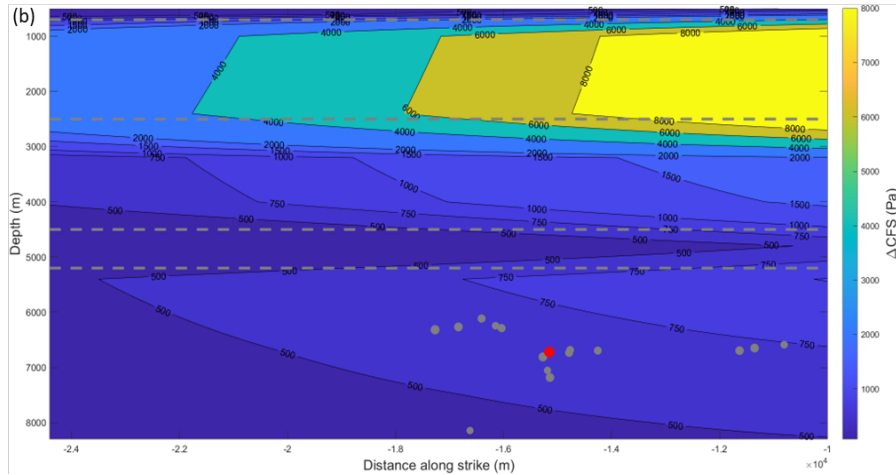


**Figure 9.**  $\Delta$ CFS of injection scenarios (a) SI-1 and (b) SI-2. Gray dashed lines separate the anhydrite/halite, sandstone, shale, limestone and basement layers (from top to bottom). The red and grey circles denote the mainshock location and neighboring seismicity, respectively. Changes in pore pressure, normal and shear stress is shown in Figure S13.

At the mainshock depth of 6.7 km, injection in sandstone (SI-1) results in a much larger volumetric strain than in limestone (SI-2) for wells located within 20 km from the mainshock (Figure S15). Interestingly, volumetric strain decreases more slowly with distance in SI-2 (limestone), and hence the volumetric strain in SI-1 actually falls below that in SI-2 beyond 20 km. Furthermore, the volumetric strain in SI-1 becomes negative beyond 25 km. This can be explained by the injection-induced deformation transitioning from expansion to compression, and the exact position of this transition is, again, governed by the intrinsic rock properties, as well as the injection parameters (Chang & Segall, 2016).

Our modeling results demonstrate the essential roles that the hydrogeological properties of the injection layer and the distance between injection and preexisting fractures play in determining the

extent of poroelastic deformation and ultimately the timing and location of induced seismicity. In the Delaware Basin, many shallow injection wells with large injection volume are located within 20 km of the mainshock, and hence our modeling results suggest that they can cumulatively cause significant poroelastic stress perturbations to the basement faults. In order to accurately assess the dominant mechanism controlling injection-induced seismicity and local and regional seismic risk, one would need clear imaging of subsurface structures, such as the hydrogeology of various rock layers and fault architecture that may act as hydraulic connections.

## CONCLUSIONS

In this work, we perform source parameter analysis of the M5.0 Mentone earthquake in the Delaware basin and explore the potential role of shallow injection wells in the triggering of this earthquake. The M5.0 event occurred on a south-dipping normal fault in the basement at a depth of 6.7 km. Although the injection depth of these wells is far from the basement faults, due to their large injection volume, poroelastic stress perturbation contributes to significant cumulative  $\Delta CFS$  of  $\sim 20$  kPa. Depending on local fault architecture, our findings suggest that the shallow injection in the region may be the primary cause of the M5.0 earthquake. Our results confirm the significance of poroelastic stress triggering over large distances, especially when the injection volume is large. Furthermore, our study highlights the effect of rock properties of injection layers in the extent of pressure and stress perturbations caused by fluid injection. In this case, injection in sandstone results in much more prominent stress perturbations than in limestone. Overall, our results have important implications for future injection operations, especially when there exists thick impermeable geologic layers between the injection and basement faults. Due to the

cumulative coupled poroelastic stress perturbation over large distances, regulators should consider the effects of fluid over an extensive region near injection sites when developing relevant operational policies.

## DATA AND RESOURCES

Injection and seismic data are obtained from the Railroad Commission of Texas and Incorporated Research Institutions for Seismology (IRIS) Data Management Center, respectively (<https://www.rrc.texas.gov/>; last accessed January 2021; <https://ds.iris.edu/wilber3/>; with the following networks: (1) the TX (Texas Seismological Network; UT Austin, 2016); (2) the US (USNSN, Albuquerque, 1990); (3) the 4T (Texas Seismological Network; UT Austin, 2018); (4) the SC (New Mexico Tech Seismic Network; New Mexico Tech, 1999); (5) the GM (U.S. Geological Survey Networks; USGS, 2016). last accessed January 2021). Seismic event catalogue information is retrieved from and the United States Geological Survey (<https://earthquake.usgs.gov/earthquakes/search/>; last access January 2021). The TexNet Earthquake Catalog can be retrieved from <https://www.beg.utexas.edu/texnet-cisr/texnet/earthquake-catalog>. The injection data used in this study can be accessed through <https://zenodo.org/record/7915695#.ZFpvlXaZOUk>. The supplemental material includes figures and tables about relevant information and results of the CAP inversion and HypoDD relocation, schematic illustration and results of the injection-induced pore pressure and poroelastic calculation, and the sensitivity analysis based on the real injection history.

437

## 438 **DECLARATION OF COMPETING INTERESTS**

439 The authors declare that there is no competing interest existed in this article.

440

## 441 **ACKNOWLEDGEMENTS**

442 The authors would like to express their sincere thanks to Dr. Rongjiang Wang and Dr. Kai Deng  
443 for their helpful discussions. This work is supported by the Natural Sciences and Engineering  
444 Research Council of Canada (Discovery Grant 2019-06482). Sincere thanks are expressed to  
445 anonymous reviewers for the helpful suggestions to our manuscript.

446

## 447 **REFERENCES**

448 Bao, X., & Eaton, D. W. (2016). Fault activation by hydraulic fracturing in western  
449 Canada, *Science* **354**, no. 6318, 1406-1409.

450

451 Barbour, A. J., Norbeck, J. H., & Rubinstein, J. L. (2017). The effects of varying injection rates in  
452 Osage County, Oklahoma, on the 2016 M w 5.8 Pawnee earthquake, *Seismol. Res. Lett.* **88**, no. 4,  
453 1040-1053.

454

455 Beauheim, R. L., & Roberts, R. M. (2002). Hydrology and hydraulic properties of a bedded  
456 evaporite formation, *J. Hydrol.* **259**, no. 1-4, 66-88.

457

458 Chang, K. W., & Segall, P. (2016). Injection-induced seismicity on basement faults including  
459 poroelastic stressing, *J. Geophys. Res.* **121**, no. 4, 2708-2726.

460

461 Deichmann, N., & Garcia-Fernandez, M. (1992). Rupture geometry from high-precision relative  
462 hypocentre locations of microearthquake clusters, *Geophys.J. Int.* **110**, no. 3, 501-517.

463

464 Deng, K., Liu, Y., & Chen, X. (2020). Correlation between poroelastic stress perturbation and  
465 multidisposal wells induced earthquake sequence in Cushing, Oklahoma, *Geophys. Res. Lett.* **47**,  
466 e2020GL089366, doi: 10.1029/2020GL089366.

467

468 Ellsworth, W. L. (2013). Injection-induced earthquakes, *Science* **341**, 1225942.

469

470 Goebel, T. H. W., Weingarten, M., Chen, X., Haffener, J., & Brodsky, E. E. (2017). The 2016  
471 Mw5. 1 Fairview, Oklahoma earthquakes: Evidence for long-range poroelastic triggering at > 40  
472 km from fluid disposal wells, *Earth Planet. Sci. Lett.* **472**, 50–61.

473

474 Goebel, T. H., & Brodsky, E. E. (2018). The spatial footprint of injection wells in a global  
475 compilation of induced earthquake sequences, *Science* **361**, 899-904.

476

Jaeger, J. C. & N. G. W. Cook (1979). *Fundamentals of Rock Mechanics*, 3rd edition, Chapman and Hall, London.

Keranen, K. M., Savage, H. M., Abers, G. A., & Cochran, E. S. (2013). Potentially induced earthquakes in Oklahoma, USA: Links between wastewater injection and the 2011 Mw 5.7 earthquake sequence, *Geology* **41**, no. 6, 699-702.

Keranen, K. M., Weingarten, M., Abers, G. A., Bekins, B. A., & Ge, S. (2014). Sharp increase in central Oklahoma seismicity since 2008 induced by massive wastewater injection, *Science* **345**, 448-451.

Keranen, K. M., & Weingarten, M. (2018). Induced seismicity, *Annu. Rev. Earth Planet. Sci.* **46**, 149–174.

Li, Z., Ripepi, N., & Chen, C. (2020). Using pressure pulse decay experiments and a novel multi-physics shale transport model to study the role of Klinkenberg effect and effective stress on the apparent permeability of shales, *J. Pet. Sci. Eng.* **189**, 107010.

Lim, H., Deng, K., Kim, Y. H., Ree, J. H., Song, T. R., & Kim, K. H. (2020). The 2017 Mw 5.5 Pohang earthquake, South Korea, and poroelastic stress changes associated with fluid injection, *J. Geophys. Res.* **125**, doi: 10.1029/2019jb019134.

498

499 Lund Snee, J. E., & Dvory, N. Z. (2020). Magnitude 5.0 earthquake shakes West Texas,  
500 *jenseriklundsnee.com*.

501

502 Makhnenko, R. Y., Riedel, J. J., & Labuz, J. F. (2011, June). Undrained plane strain compression  
503 of shale, in *45th US Rock Mechanics/Geomechanics Symposium*, OnePetro.

504

505 Rothert, E., & Shapiro, S. A. (2007). Statistics of fracture strength and fluid-induced  
506 microseismicity, *J. Geophys. Res.* **112**.

507

508 Rudnicki, J. W. (1986). Fluid mass sources and point forces in linear elastic diffusive solids, *Mech.*  
509 *Mater.* **5**, no. 4, 383-393.

510

511 Sheng, Y., Pepin, K. S., & Ellsworth, W. L. (2022). On the depth of earthquakes in the Delaware  
512 Basin: A case study along the Reeves–Pecos county line, *Seismol. Rec.* **2**, no. 1, 29–37.

513

514 Skoumal, R. J., Barbour, A. J., Brudzinski, M. R., Langenkamp, T., & Kaven, J. O. (2020). Induced  
515 seismicity in the Delaware basin, Texas, *J. Geophys. Res.* **125**, no. 1, doi: 10.1029/2019JB018558.

516

Skoumal, R. J., Kaven, J. O., Barbour, A. J., Wicks, C., Brudzinski, M. R., Cochran, E. S., & Rubinstein, J. L. (2021). The induced Mw 5.0 March 2020 west Texas seismic sequence, *J. Geophys. Res.* **126**, no. 1, e2020JB020693.

Suarez-Rivera, R., & Fjær, E. (2013). Evaluating the poroelastic effect on anisotropic, organic-rich, mudstone systems, *Rock Mech. Rock Eng.* **46**, no. 3, 569-580.

Tung, S., Zhai, G., & Shirzaei, M. (2021). Potential link between 2020 Mentone, West Texas M5 earthquake and nearby wastewater injection: implications for aquifer mechanical properties, *Geophys. Res. Lett.* **48**, no. 3, doi: 10.1029/2020GL090551.

Waldhauser, F., & Ellsworth, W. L. (2000). A double-difference earthquake location algorithm: Method and application to the northern Hayward fault, California, *Bull. Seismol. Soc. Am.* **90**, 1353–1368.

Wang, R., & Kümpel, H. J. (2003). Poroelasticity: Efficient modeling of strongly coupled, slow deformation processes in a multilayered half-space, *Geophysics*, **68**, 705-717.

Yeck, W. L., Weingarten, M., Benz, H. M., McNamara, D. E., Bergman, E. A., Herrmann, R. B., ... & Earle, P. S. (2016). Far-field pressurization likely caused one of the largest injection induced

537 earthquakes by reactivating a large preexisting basement fault structure, *Geophys. Res. Lett.* **43**,  
538 no. 19, 10-198.

539

540 Zhai, G., Shirzaei, M., & Manga, M. (2021). Widespread deep seismicity in the Delaware Basin,  
541 Texas, is mainly driven by shallow wastewater injection, *Proc. Natl. Acad. Sci.* **118**, no. 20, doi:  
542 10.1073/pnas.2102338118.

543

544 Zhao, L. S., & Helmberger, D. V. (1994). Source estimation from broadband regional  
545 seismograms, *Bull. Seismol. Soc. Am.* **84**, no. 1, 91-104.

546

547 Zhu, L., & Rivera, L. A. (2002). A note on the dynamic and static displacements from a point  
548 source in multilayered media, *Geophys. J. Int.* **148**, 619–627.

549

550 Zhu, W., & Beroza, G. C. (2019). PhaseNet: a deep-neural-network-based seismic arrival-time  
551 picking method, *Geophys. J. Int.* **216**, no 1, 261-273.

552

553 Zoback, M. D. (2010). *Reservoir geomechanics*, Cambridge university press, p. 156.